Validation of near infrared spectroscopic (NIRS) imaging using programmable phantoms

Randall L. Barbour[1,2], Rehman Ansari[1,2], Rabah Al abdi[2], Harry L. Graber[1,2], Mikhail B. Levin[2], Yaling Pei[1], Christoph H. Schmitz[3], Yong Xu[1,2]

1. NIRx Medical Technologies LLC., 15 Cherry Lane, Glen Head, NY 11545
2. Department of Pathology, SUNY Downstate Medical Center, 450 Clarkson Avenue, Brooklyn, NY 11203
3. Department of Neurology, Charité – Universitätsmedizin, Berlin, Germany

ABSTRACT

For much of the past decade, we have developed most of the essential hardware and software components needed for practical implementation of dynamic NIRS imaging. Until recently, however, these efforts have been hampered by the lack of calibrating phantoms whose dynamics substantially mimic those seen in tissue. Here we present findings that document the performance of a dynamic phantom based on use of twisted nematic liquid crystal (LC) technology. Programmable time courses of applied voltage cause the opacity of the LC devices, which are embedded in a background matrix consisting of polysiloxane (silicone) admixed with scattering and absorbing materials, to vary in a manner that mimics the spatiotemporal hemodynamic pattern of interest. Methods for producing phantoms with selected absorption and scattering, internal heterogeneity, external geometry, hardness, and number and locations of embedded LCs are described. Also described is a method for overcoming the apparent limitation that arises from LCs being mainly independent of the illumination wavelength. The results presented demonstrate that: the opacity vs. voltage response of LCs are highly stable and repeatable; the dynamic phantom can be driven at physiologically relevant speeds, and will produce time-varying absorption that follows the programmed behavior with high fidelity; image time series recovered from measurements on the phantom have high temporal and spatial location accuracy. Thus the dynamic phantom can fill the need for test media that practitioners may use to confirm the accuracy of computed imaging results, assure the correct operation of imaging hardware, and compare performance of different data analysis algorithms.

KEYWORDS: Calibrating phantom; Tissue-simulating phantom; NIRS imaging; Dynamic imaging; Hemodynamic response; Liquid crystal cells; Twisted nematic liquid crystals.

1. INTRODUCTION

Common to all quantitative analytical methods is the need for calibrators that serve to verify short and long-term measurement reliability, serve as training vehicles, and provide insight into system troubleshooting. Calibrators in the form of imaging phantoms are routinely used for all structural imaging methods. In the case of studies that explore dynamic phenomena, it is highly desirable to employ phantoms whose phenomenology can be adjusted in a manner that substantially duplicates the expected response observed from tissue. Extension of this requirement to NIRS studies argues for a phantom that substantially resembles real tissue in terms of its geometry, background optical properties and relevant contrast dynamics (i.e., spectroscopic properties and temporal response).

Consideration of these requirements brings to mind two possible strategies: a fluidic approach, or, alternatively, use of electrochromic materials whose optical properties can be reversibly adjusted through variations in the driving potential. Here we extend previous reports[1],[2] that introduced the concept of employing the second approach as a general strategy to mimic a broad range of dynamic optical phenomenology that includes absorption, scattering, and fluorescent or bioluminescent properties. Electrochromic materials constitute a broad class of materials that range from liquid crystals to conducting polymers.[3,4] The choice of which material is most suitable will depend on the desired temporal response,

spectral properties, long term stability and a host of practical issues (e.g., nonrecurring and recurring costs, ease of customization, etc.).

In the late 1990s, our group first demonstrated the feasibility of extending the NIRS imaging technique to allow for the capture of an image time series.[5] Central to this capability were two developments. One dealt with the specification of a stable reconstruction method that overcame sensitivities inherent to the uncertainties of practical measurement (*e.g.*, incomplete knowledge of tissue boundary conditions, internal optical properties, optical system efficiency, etc.).[6] The second defined an instrument design that enabled the capture of emission profiles on a sub-second time scale while having a very large dynamic range, thereby enabling the collection of full view tomography measurements including measures co-located with the source.[7] Together, these developments rendered feasible dynamic NIRS imaging that today has attracted a growing following.[8,9,10,11,12,13] While the basic system design continues to undergo advancements in both hardware performance[14] and data analysis,[15] mainly lacking has been the availability of a calibrating phantom whose dynamics substantially mimic those seen in tissue.

Here we present findings that document the performance of a dynamic phantom based on use of twisted nematic (TN) liquid crystal technology. Results obtain document that the considered approach provide for a fully programmable phantom having reversible optical properties that can duplicate a host of complex hemodynamic responses with excellent reproducibility, millisecond response times, large dynamic range, long operating times (>20,000 hours) and shelf-life (multiyear).

2. METHODS

2.1. Phantom construction

Molds of anatomically shaped structures were used to construct phantoms composed of a two-component tin-catalyzed condensation cure silicone mixture containing added TiO_2 and India ink. To avoid excessive adhesion of additives to the mixing containers, they were first added to the bulk polydimethylsiloxane material and vigorously stirred using an impeller mixer to achieve homogeneous slurry. The mixture was subsequently degassed, combined with catalyst, mixed and degassed again. The binary product was then poured into the mold that contained the desired number of LC cells, which were pre-positioned using a scaffolding of fine wires, and allowed to cure for 48 hours. The resultant material had a durometer value of approximately 30. When appropriate, phantoms were constructed in stages to produce heterogeneous structures. In the case of a head phantom, this included efforts that produced an anatomically contoured cortex covered by a thin transparent silicone layer representing CSF, all of which was subsequently encased in a commercially available plastic skull. Reported here are results obtained from a dual-breast phantom containing two cells per breast, and a head phantom containing 8 embedded cells. The optical coefficients of the background silicone medium doped with the indicated additives were approximately 8 cm^{-1} for μ_s' and 0.05 cm^{-1} for μ_a.

2.2. Phantom control

Figure 1 shows a schematic of the functional elements that provide for programmable control of the LC cell's opacity. Analogue control is achieved using a balanced modulator whose primary signals are generated using a National Instruments data acquisition card (model no. USB 6211) that is controlled by a LabView program. This serves to adjust cell opacity according to user-defined time-dependent functions. Equivalent spectral encoding is accomplished through a time multiplexing scheme that serves to interleave wavelength-dependent absorbencies. In the case of a two-wavelength measurement, cell opacity is adjusted to correspond to the absorbance at wavelength 1, held constant for a single tomographic scan, and subsequently adjusted to the absorbance at wavelength 2 for the next scan. By applying this interleaving scheme to subsequent scans, and adjusting opacities, time-dependent equivalent spectral responses can be achieved. This interleaving scheme is diagrammed in Figure 2, which depicts the synchronization of the imager and phantom timing operations in greater detail, and in Figure 3, which also shows how LC driving functions are derived from a model of hemodynamic behavior.

Shown in Figure 4 is a screenshot of the GUI we have developed to control the phantom. Motivating its design is the expected need for routine quality assurance checks (e.g., imager performance), assessment of algorithm performance (image recovery and feature extraction), and validation checks to distinguish artifacts from true image features. Supporting quality assurance are various library files (e.g., trigonometric functions, square waves, etc.) that serve to

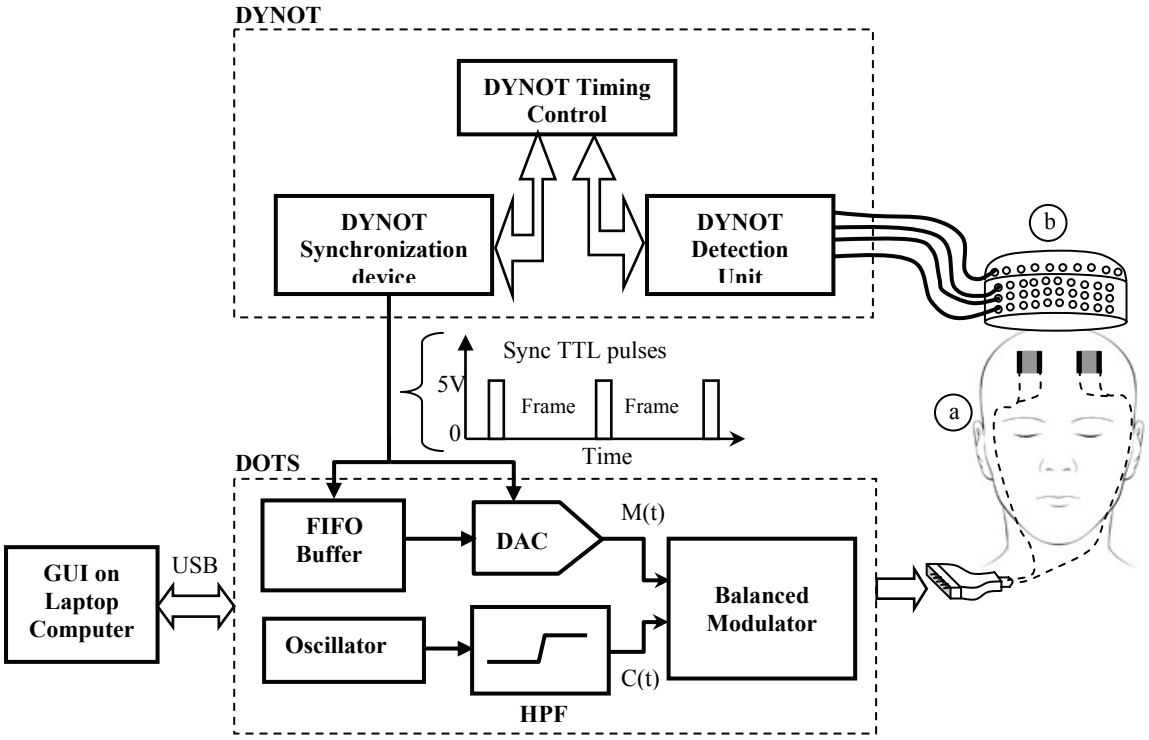

Figure 1. Functional elements of dynamic optical tissue simulator (DOTS) instrumentation and its connectivity to the DYNOT imaging system.

DYNOT Sub-components (see Ref. 7): The DYNOT synchronization device sends a TTL (Transistor-Transistor logic) pulse to the DOTS controller at the start of each image acquisition cycle, causing the latter to adjust the voltage applied to the LC cells in the dynamic phantom. This produces the synchronization of medium properties with data acquisition depicted in Fig. 3. The DYNOT detection unit receives re-emitted light signals from the target medium (dynamic phantom, in this example) and converts them to voltage values proportional to the light intensity. The DYNOT timing control coordinates the illumination of the target and data acquisition.

DOTS Sub-components: GUI: Graphical user interface (see Fig. 4). FIFO: First in first out memory, which stores the pre-programmed LC driving function and outputs successive values when prompted by the TTL pulses from the DYNOT. DAC: Digital-to-analog converter; this produces an analogue voltage signal, proportional in magnitude to the most recent FIFO output, that determines the amplitude of the AC signal passed to the LC cells. HPF: High pass filter, to remove the DC component of the oscillator output, leaving a pure AC carrier signal. The balanced modulator output, which is the LC cell input, is an AC signal whose frequency and phase are determined by the oscillator, with an amplitude determined by the DAC output. M(t), C(t): modulating and carrier signal.

Target medium – DYNOT measuring head interface: (a) LC cells embedded in a silicone head. Active surface area of each LC cell is approximately 1 cm^2. (b) Measuring helmet with spring loaded optical fibers.

quantify the temporal and equivalent spectral accuracy, and from which simple or complex hemodynamic responses can be derived. Alternatively, the user can upload a specific file corresponding to a raw wavelength measurement or to a hemoglobin time series. Additionally, a graphical interface is provided to support generation of user-defined functions. Verification of image resolution can be made by operating multiple cells simultaneously. In its current hardware configuration, we can support the driving of a maximum of eight LC cells in parallel.

2.3. Data acquisition using a 128 channel dual-breast dynamic near-infrared optical tomography (DYNOT) imager

Figure 5 shows a photograph of the dual-breast imaging head used to explore the breast phantom. Each measuring head supports 32 delivery and 64 collecting optics that are situated within adjustable elements that constitute the top and bottom components of the head. The overall unit functions similar to a hand having an adjustable wrist and fingers. Additionally, each finger member of the measuring head is fitted with a semiconductor strain gauge to allow for precise adjustment of the contact pressure. Basic imager functionality is similar to that described previously. The system provides for simultaneous dual-wavelength (760, 830 nm) illumination using a time-multiplexing scheme, frequency encoding and on-the-fly gain adjustment. System control is achieved through a LabView interface that supports a broad range of system diagnostics and visualization features.

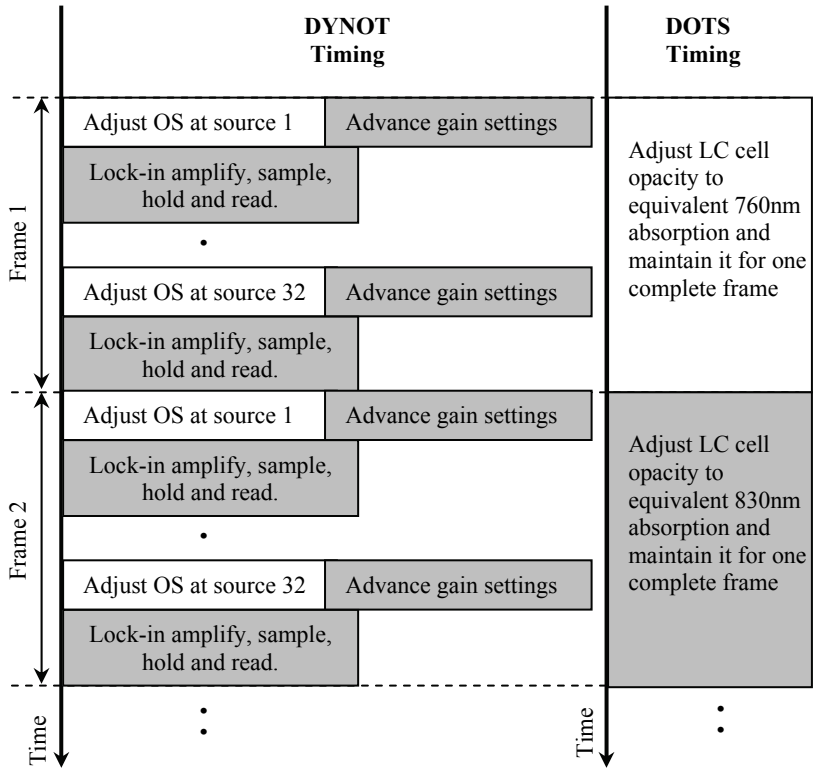

Figure 2. Synchronization scheme between DYNOT's frame acquisition (see Ref. 7) and DOTS controlling of the LC cell opacity. OS: Optical switch.

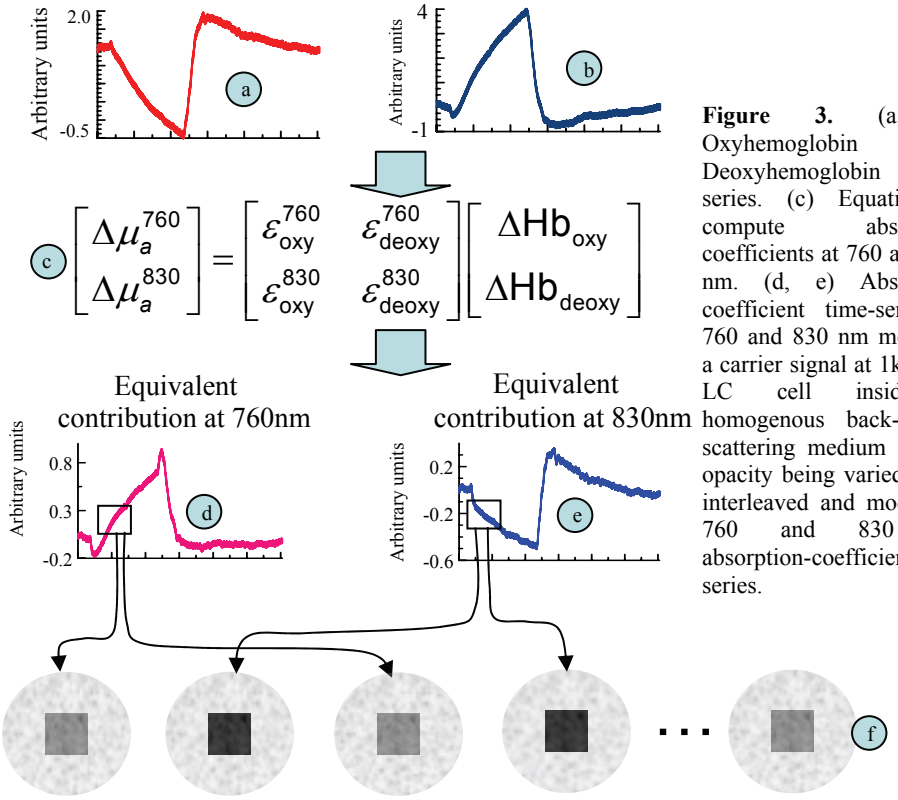

Figure 3. (a, b) Oxyhemoglobin and Deoxyhemoglobin time-series. (c) Equation to compute absorption coefficients at 760 and 830 nm. (d, e) Absorption coefficient time-series at 760 and 830 nm modulate a carrier signal at 1kHz. (f) LC cell inside a homogenous back-ground scattering medium and its opacity being varied by an interleaved and modulated 760 and 830 nm absorption-coefficient time series.

2.4. Image reconstruction

For each acquired phantom time series, dual-wavelength data were paired according to the scheme illustrated in Fig. 3, preprocessed using a low-pass filter and a polynominal fitting routine to correct for slow variations in signal baseline, and normalized to the co-located signal to compensate for small fluctuations in optical power. Wavelength dependent images were computed using the Normalized Difference Method of Pei *et al*., and from these the corresponding hemoglobin time series results were subsequently computed. Where appropriate, images of GLM coefficients were computed using the original Hb time series as the model function.

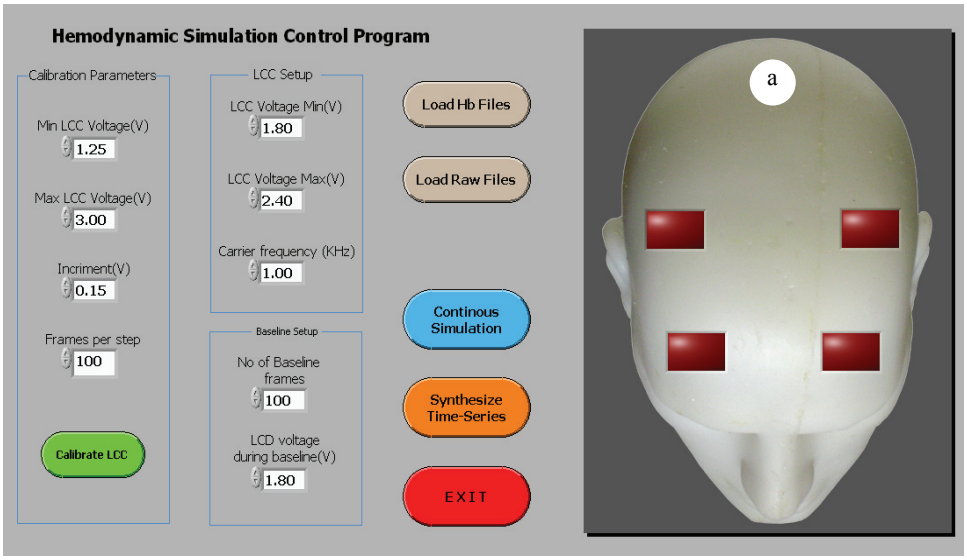

Figure 4. Screenshot of DOTS graphical user interface. (a) Displays the real-time changes in the opacities of the LC cells that are embedded in silicone based phantom.

3. RESULTS

3.1. Opacity Response of LC Cell

Figure 6 shows the wavelength-dependent opacity response of the LC cell as a function of applied voltage. Points shown are the mean value obtained for 50 consecutive time points when the LC cell was operated at a fixed voltage, normalized to the maximum transmittance seen. Standard deviation error bars are also indicated but are within the width of the data points, indicating that the precision of measurement is excellent (CV typically < 0.2%) over the full operating range of the cell. Note that here the wavelength-dependent response is the true response and not an equivalent one as depicted in Fig. 3. When the data are expressed as unnormalized amplitudes, the two curves are mainly parallel and differ by less than 10% in amplitude. Shown in Figure 7 is comparison of results obtained from two of the four LC cells contained within the breast phantom (transmittance measurement) to equivalent measures made in the absence of the surrounding attenuating medium, as a function of applied voltage. A linear response is seen, indicating that the only consequence of the surrounding scattering medium is to reduce the attenuating effect of variations in cell opacity. This reduction is reasonable, given the expectation that a surrounding scattering medium serves to establish many propagating paths, of which only a portion will pass through the cell before exiting the medium. Also seen is a systematic bias in attenuation between the two breasts. This is expected and results from the fact that the two fabricated breasts have slightly different thicknesses.

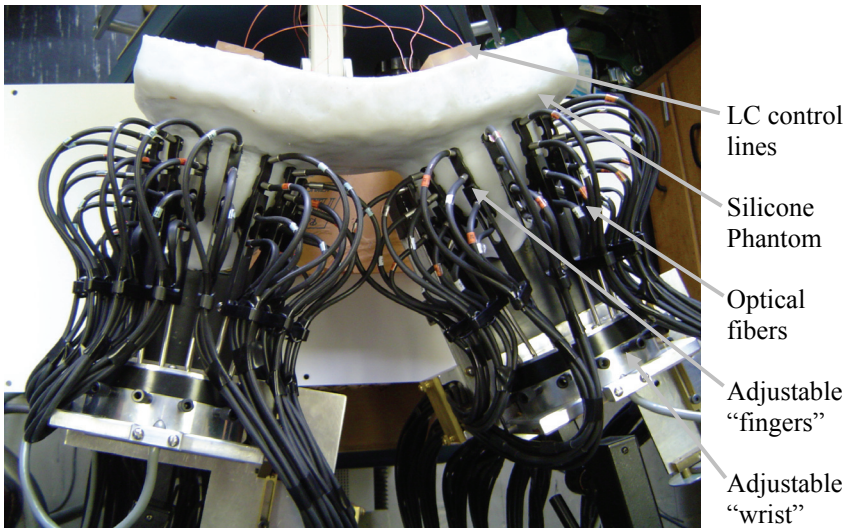

Figure 5. Dual-breast measuring head with breast phantom containing LC cells.

In Figure 8 we document the temporal response of the LC cell to multiple variations in contrast voltage. The response seen is a step function having settling time << than the temporal resolution of the imager. Experience with LC cells of this type indicate that the 50% rise time for the cell is in fact < 1 msec.

3.2. Equivalent Hemodynamic Response of LC Cell

Figure 9 shows the response to three successive transmittance measurements made in air compared to the selected driving function (hemoglobin response to cuff ischemia) synthesized according to the scheme depicted in Fig. 3. Comparison reveals that the measured time-dependent Hb response is highly repeatable, and is nearly identical to the driving function.

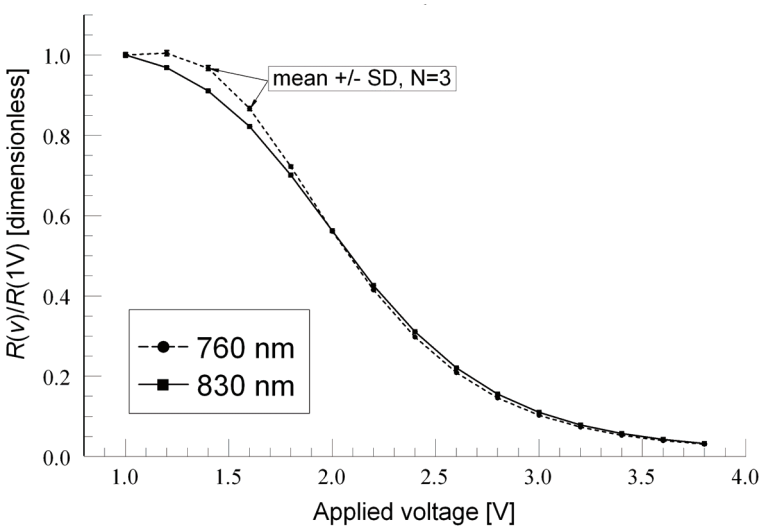

Figure 6. Voltage-dependent opacity (*i.e.*, fraction of normally incident light transmitted for a selected LC, for both measurement wavelengths.

3.3. Time series imaging of hemoglobin response

Figures 10-12 show results obtained from tomographic imaging studies. Shown in Figure 10(a) is the FEM mesh used for reconstruction of breast imaging results, containing two inclusions whose locations are substantially similar to the LC cells contained in the real breast phantom. The physical dimensions of the model are 10 cm from front to back (*i.e.*, nipple to chest wall), 6 cm from bottom to top, and 12 cm from left to right. Fig. 10(b) shows the results from a computer simulation when the absorbance of the inclusions is 100% greater than the background, while Fig. 10(c) shows the corresponding results, thresholded to 50% of the maximum image value, obtained from an experiment on the breast phantom. Specific results shown in Fig. 10(c) correspond to findings obtained from a GLM computation applied to driving the breast phantom according to the cuff ischemia time series shown in Fig. 9, using cell voltages that effect maximum contrast. Several factors are demonstrated by these results. The result in Fig. 10(b) indicates that image recovery using the NDM method can be obtained with excellent spatial location and extent. Fig. 10(c) shows that substantially equivalent results can be obtained from the phantom. This demonstrates that high quality tomographic measurements are obtainable using the DYNOT imager and that the

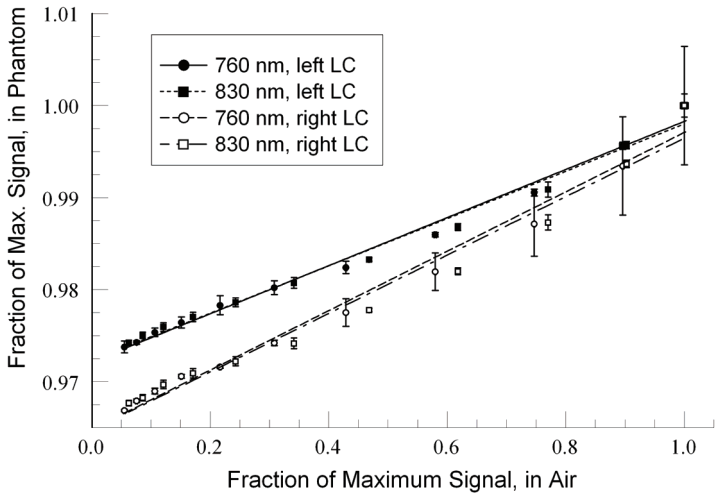

Figure 7. Linear relation between measured opacities for a non-embedded LC and for two LCs embedded in a silicone dynamic phantom.

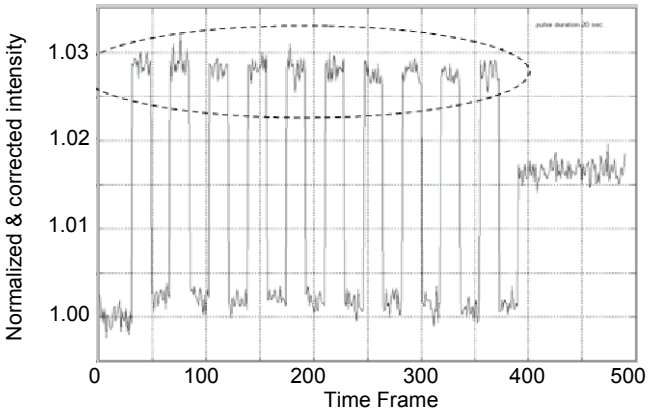

Figure 8. Measured LC transmission (relative scale), as applied voltage alternates between a low (circled data points) and high value. Stability, repeatability, and effectively instantaneous response of the LC are demonstrated.

performance of the LC cell within the phantom substantially duplicates the hemodynamic response of the driving function.

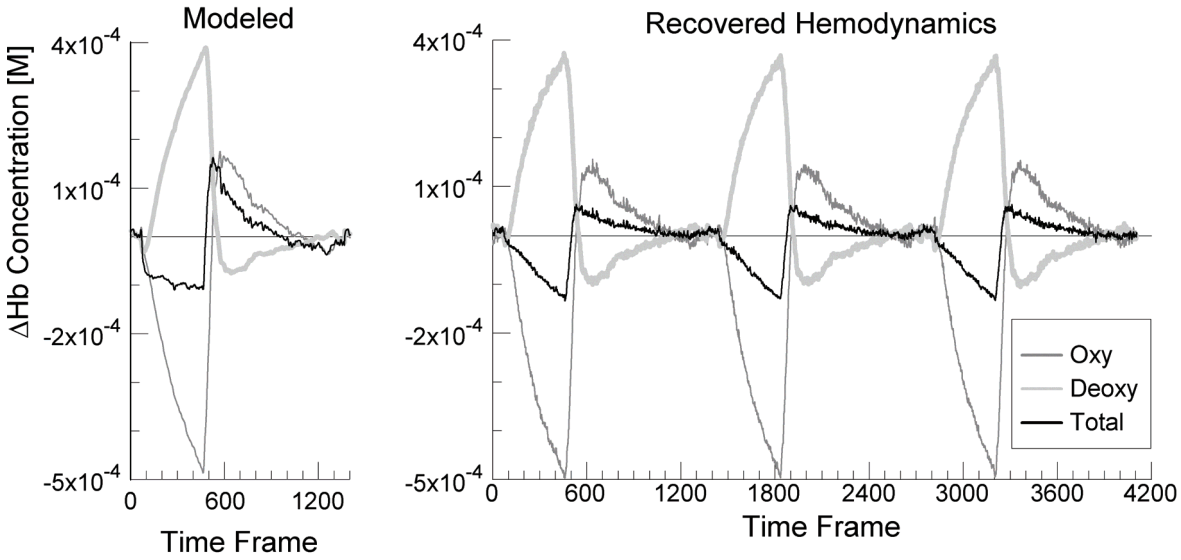

Figure 9. Modeled hemodynamic behavior (left), and functions recovered from a non-embedded LC cell (right), for three successive measurement cycles. Results demonstrate the linearity and repeatability of the cell's performance.

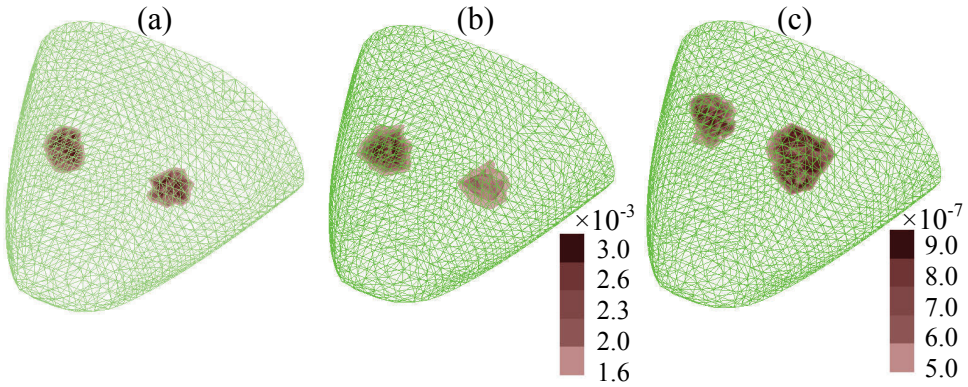

Figure 10. (a) FEM mesh used for reconstruction of breast imaging results, containing two inclusions at locations substantially similar to the LC cells in the silicone breast phantom. (b) Results from a computer simulation, with absorbance of the inclusions 100% greater than the background. (c) Corresponding results, thresholded to 50% of the maximum image value, obtained from an experiment on the breast phantom.

Results shown in Figure 11 explore the sensitivity of recovered images to variations in LC cell contrast. Shown are the amplitudes of GLM coefficient values from transects taken through the center of the reconstructed image. Results shown in Figure 12 is a replot of data from Figs. 6 and 11, demonstrating that the amplitude of the reconstructed image varies linearly with the LC cell opacity.

Results in Figure 13 document our ability to explore hemodynamic responses in complex backgrounds based on back-reflection measurements. Here we have employed a heterogeneous head phantom comprised of a topographically realistic cortex, a superficial clear layer modeling CSF and a surrounding skull composed of plastic. Identified in the figure is the response seen from selected source-detector pairs to repeated changes in blood volume. Inspection shows that the response is highly repeatable. Shown in Figure 14 are the corresponding reconstructed image results in the case

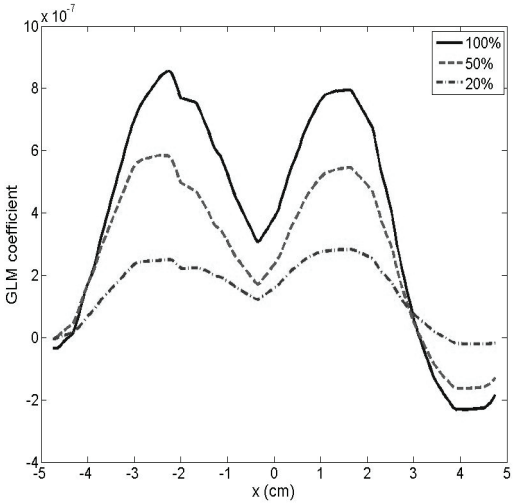

Figure 11. One-dimensional sections through 3D spatial maps of computed GLM coefficients, for experimental result of the type shown in Fig. 10(c). The three curves correspond to different ranges of LC opacity.

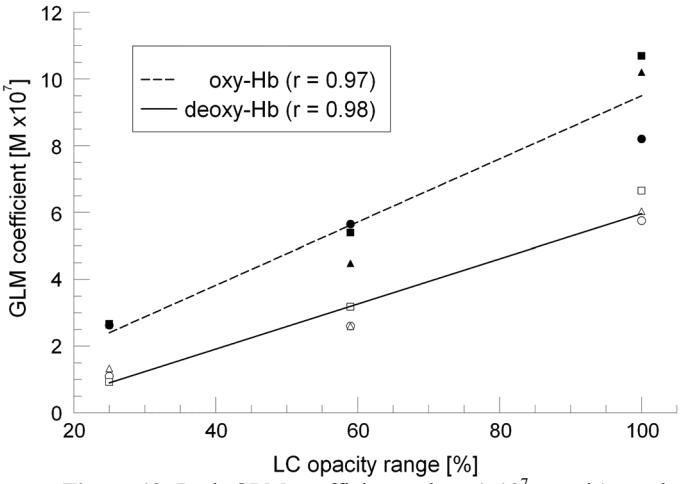

Figure 12. Peak GLM coefficient values ($\times 10^7$, y-axis) vs. the corresponding ranges of LC opacities employed in the experimental measurements (x-axis). Each measurement was repeated three times; individual symbols indicate the GLM coefficients for one of the replicates.

where the background medium is represented by a segmented MR map [Fig. 14(a)]. Shown in Fig. 14(b) is a volume-rendered map depicting the location of the LC cell. Shown in Fig. 14(c) is a spatial map of the computed GLM coefficient corrected for distortion common to back-reflection measurement using the image correction method described by Graber *et al.*[16] Fig. 14(d) shows the time course of the recovered dynamics in the inclusion region (LC cell) and background. Inspection shows that the accuracy of location quality of recovered dynamics is excellent.

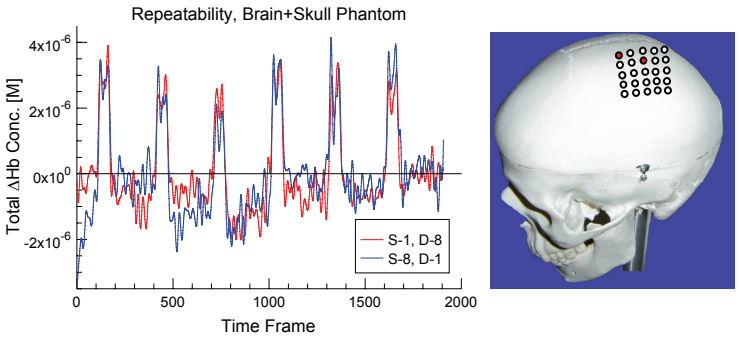

Figure 13. Measured responses for selected source-detector pairs, from an experiment performed on a heterogeneous head phantom comprised of a topographically realistic cortex, a superficial clear layer modeling CSF and a surrounding skull composed of polyvinyl chloride.

4. DISCUSSION

Here we have reported on the performance characteristics of a reversible dynamic phantom based on TN liquid crystal cell technology. It is appreciated that cells of this type typically have a rather flat spectral response over the wavelength range of interest, and on its surface it might seem that this technology would not be suitable to accomplish the hemodynamic responses demonstrated here. We have overcome this limitation by implementing a time-multiplexing approach that produces the corresponding wavelength dependent absorbance changes within a time frame that makes the assumption of stationarity fully justified. As originally discussed by Barbour, it is understood that electrochromic cell technology in general can be adopted in many ways to provide an effective platform for validating dynamic optical imaging findings, benchmarking system performance, etc. In addition, cells can be configured in many ways to allow for evaluation of other optical responses of interest, including light scatter, fluorescence, and bioluminescence. Still another consideration refers to the quantitative extension of measures based on 2D cell geometry to reconstructed images that reveal an apparent 3D inclusion. Much of this effect is a result of the limits on spatial resolution represented by diffuse

optical tomography. This said, we believe it is still appropriate for many applications to treat the reconstructed image as representing the response that would be seen from an equivalent 3D inclusion. For instance, as shown in Figure 10, we find that the principal image features seen from the LC cell substantially duplicate those seen when modeling a 1.2 cm diameter inclusion. This raises the following question. Using the maximum contrast response of the LC cell, how much of a change in hemoglobin concentration does this correspond to in relation to an inclusion having a diameter of 1.2 cm? We have evaluated this and the answer is approximately 30 μM. Because we are modeling equivalent responses, it is understood that this value will depend somewhat on where in the medium the cell is located and how the physical measurement is made (i.e., transmittance, backreflection). These dependences, however, can be calibrated and thus we anticipate that the considered approach should have broad applicability to many practical studies.

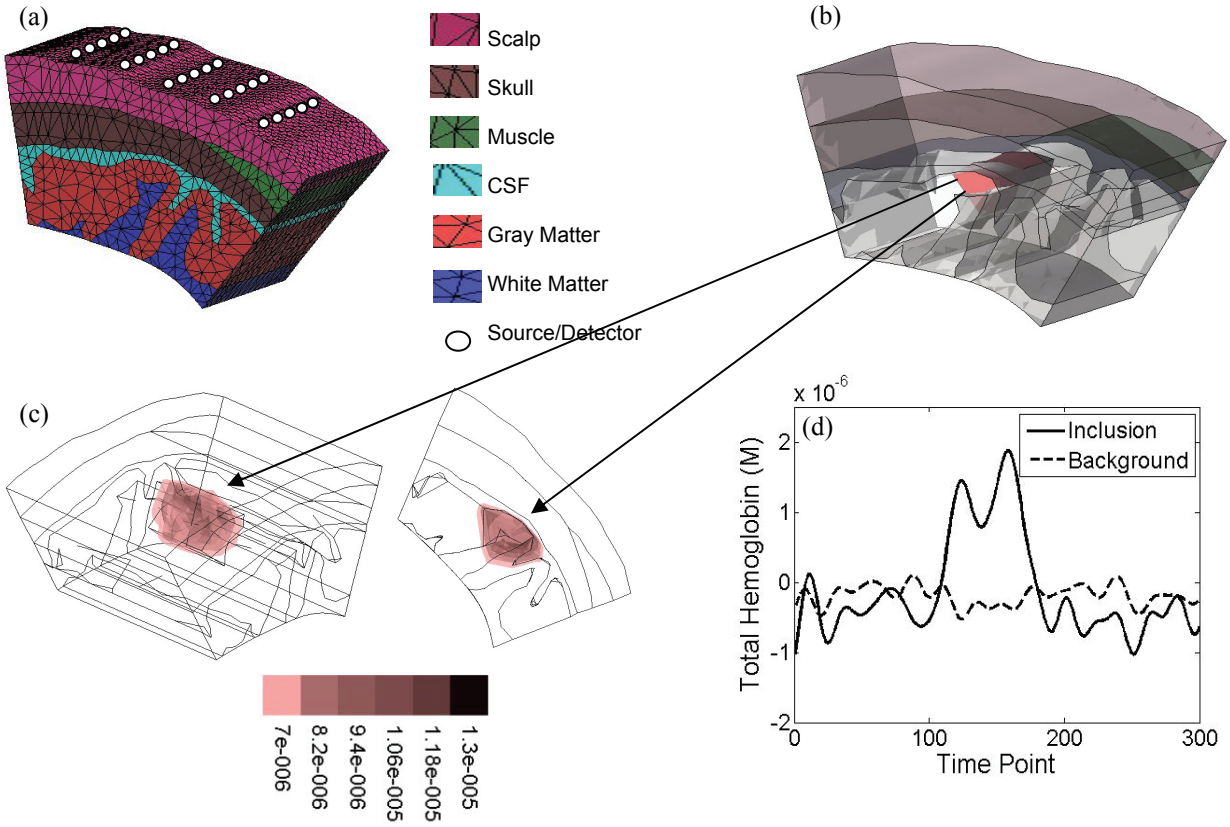

Figure 14. (a) Segmented MR brain map containing indicated tissue types. (b) Volume rendered image showing location of dynamic inclusion embedded in gray matter. (c) Reconstructed image of dynamic response (GLM map) obtained using methods available in NAVI (Ref. 15). (d) Time-dependent pixel response seen in background and inclusion, revealing excellent recovery of blood volume change.

5. REFERENCES

[1] Barbour, R.L., Graber, H.L., Xu, Y., Pei, Y., Ansari, R., Levin, M.B., and Farber, M., "Diffuse Optical Tissue Simulator (DOTS): An experimental calibrating system for functional DOT imaging," Poster No. 76 at Fifth Inter-Institute Workshop on Optical Diagnostic Imaging from Bench to Bedside at the National Institutes of Health (Bethesda, MD, September 25-27, 2006). http://otg.downstate.edu/Publication/BarbourNIH06A.pdf.

[2] Barbour, R.L., "Electronically Modulated Dynamic Optical Phantoms for Biomedical Imaging," International Publication No. WO 2006/135850 A3, December 21, 2006. http://www.wipo.int/pctdb/en/wo.jsp?wo=2006135850&IA=WO2006135850&DISPLAY=DOCS.

[3] Donald, A.M., Windle, A.H., and Hanna, S., [Liquid Crystalline Polymers, 2nd Ed.], Cambridge University Press (2006).
[4] Case Western Reserve University Dept of Macromolecular Science and Engineering "Virtual Textbook" http://plc.cwru.edu/tutorial/enhanced/files/credits.htm
[5] Barbour, R.L., Graber, H.L., Schmitz, C.H., Pei, Y., Zhong, S., Barbour, S.-L. S., Blattman, S., and Panetta, T., "Spatio-Temporal Imaging of Vascular Reactivity by Optical Tomography," in *Proceedings of Inter-Institute Workshop on* In Vivo *Optical Imaging at the NIH*, A. H. Gandjbakhche, ed. (Optical Society of America, Washington, DC 1999), pp. 161-166. http://otg.downstate.edu/Publication/BarbourNIH99.pdf.
[6] Pei, Y., Graber, H.L., and Barbour, R.L., "Influence of systematic errors in reference states on image quality and on stability of derived information for DC optical imaging," Applied Optics 40(31), 5755-5769 (2001).
[7] Schmitz, C.H., Löcker, M., Lasker, J.M., Hielscher, A.H., and Barbour, R.L., "Instrumentation for fast functional optical tomography," Review of Scientific Instruments 73(2), 429-439 (2002).
[8] Everdell, N.L., Gibson, A.P., Tullis, I.D.C., Vaithianathan, T., Hebden, J.C., and Delpy, D.T., "A frequency multiplexed near-infrared topography system for imaging functional activation in the brain," Review of Scientific Instruments 76(9), 093705 (2005).
[9] Boverman, G., Fang, Q., Carp, S.A., Miller, E.L., Brooks, D.H., Selb, J., Moore, R.H., Kopans, D.B., and Boas, D.A., "Spatio-temporal imaging of the hemoglobin in the compressed breast with diffuse optical tomography," Physics in Medicine and Biology 52, 3619-3641 (2007).
[10] Lee, J., Saltzman, D.J., Cerussi, A.E., Gelfand, D.V., Milliken, J., Waddington, T., Tromberg, B.J., and Brenner, M., "Broadband diffuse optical spectroscopy measurement of hemoglobin concentration during hypovolemia in rabbits," Physiological Measurement 27(8), 757-767 (2006).
[11] Zhou, C., Choe, R., Shah, N., Durduran, T., Yu, G., Durkin, A., Hsiang, D., Mehta, R., Butler, J., Cerussi, A., Tromberg, B.J., and Yodh, A.G., "Diffuse optical monitoring of blood flow and oxygenation in human breast cancer during early stages of neoadjuvant chemotherapy," J. Biomedical Optics 12(5), 051903 (2007).
[12] Sunar, U., Quon, H., Durduran, T., Zhang, J., Du, J., Zhou, C., Yu, G., Choe, R., Kilger, A., Lustig, R., Loevner, L., Nioka, S., Chance, B., and Yodh, A.G., "Noninvasive diffuse optical measurement of blood flow and blood oxygenation for monitoring radiation therapy in patients with head and neck tumors: a pilot study," J. Biomedical Optics 11(6), 064021 (2006).
[13] Culver, J.P., Siegel, A.M., Franceschini, M.A., Mandeville, J.B., and Boas, D.A., "Evidence that cerebral blood volume can provide brain activation maps with better spatial resolution than deoxygenated hemoglobin," Neuroimage 27(4), 947-959 (2005).
[14] Lasker, J.M., Masciotti, J.M., Schoenecker, M., Schmitz, C.H. and Hielscher, A.H., "Digital-signal-processor-based dynamic imaging system for optical tomography," Review of Scientific Instruments 78(8), 083706 (2007).
[15] Pei, Y., Wang, Z., Xu, Y., Graber, H.L., Monteiro, R., and Barbour, R.L. "NAVI: A problem solving environment (PSE) for NIRS data analysis," Poster No. 114 at Fifth Inter-Institute Workshop on Optical Diagnostic Imaging from Bench to Bedside at the National Institutes of Health (Bethesda, MD, September 25-27, 2006). http://otg.downstate.edu/Publication/PeiNIH06B.pdf.
[16] Graber, H.L., Xu, Y., Pei, Y., and Barbour, R.L., "Spatial deconvolution technique to improve the accuracy of reconstructed three-dimensional diffuse optical tomographic images," Applied Optics 44(6), 941-953 (2005).